Relativistic three-body scattering and the $D^0D^{*+} - D^+D^{*0}$ system

Xu Zhang*

CAS Key Laboratory of Theoretical Physics, Institute of Theoretical Physics, Chinese Academy of Sciences, Beijing 100190, China

(Received 12 February 2024; accepted 9 April 2024; published 6 May 2024)

Scattering amplitudes involving three-particle scattering processes are investigated within the isobar approximation which respects constraints from two- and three-body unitarity. The particular system considered is the $D^0D^{*+} - D^+D^{*0}$, where the D^{*+} (D^{*0}) enters as a p-wave $D^+\pi^0$ or $D^0\pi^+$ ($D^0\pi^0$ or $D^+\pi^-$) resonance. The interaction potentials in the coupled-channel $D^0D^{*+} - D^+D^{*0}$ system contain the σ, ρ, ω, and π-exchange. The analytic continuation of the amplitudes across the three-body unitary cuts is investigated to search for poles on the unphysical Riemann sheets. Associated with an unstable particle D^{*+} (D^{*0}) is a complex two-body unitarity cut, through which one can further analytically continue into another unphysical Riemann sheet. Dynamical singularities emerged from the π-exchange potential are stressed. The pole generated from the $D^0D^{*+} - D^+D^{*0}$ interaction and its line shape in $D^0D^0\pi^+$ break-up production are in agreement with double-charmed tetraquark T_{cc}^+ observed by the LHCb Collaboration.

DOI: 10.1103/PhysRevD.109.094010

I. INTRODUCTION

A large number of new hadron states have been observed experimentally, especially the so-called exotic states which are beyond the scope of the conventional quark model. For a recent review on the experimental and theoretical status of such exotic states, see Refs. [1–13]. Considerable progress has been achieved recently in calculating the hadron spectrum based on first principle lattice quantum chromodynamics (QCD) [14–21]. Hadron spectrum emerges from the internal dynamics of the QCD degrees of freedom. The resonance mass characterizes the long-distance dynamics of quarks and gluons, its width manifests on the coupling to the decay channels. To extend our knowledge of this aspect of QCD phenomenology, it is necessary to analytically continue the partial wave amplitudes into the unphysical region and extract resonance parameters from experimental data or lattice QCD simulations, as resonances manifesting as pole singularities in the scattering amplitudes [22–30].

Many of those newly observed exotic states can be interpreted as a deuteron like molecular states generated from various hadron-hadron interactions. Among those newly observed exotic states, the most notable example in charmonium sector is the $D^0\bar{D}^{*0} - D^{*0}\bar{D}^0$ molecule candidate $X(3872)$ [31]. However, as discussed in Refs. [32–36], the treatment of pions may differ from ordinary chiral perturbative theory or the NN theory of Refs. [37,38]. First, since the $\bar{D}^{*0}(D^{*0}) - \bar{D}^0(D^0)$ hypefine splitting and the π^0 mass is nearness, the π^0-exchange will be characterized by an anomalously small scale and generate anomalously long-range effect. This suggests that if the binding energy of $X(3872)$ is not much smaller than its upper limit, the π^0 should be included as explicit degrees of freedom [32,33]. Second, the $\bar{D}^{*0}$ (D^{*0}) is very close to the $\bar{D}^0\pi^0$ $(D^0\pi^0)$ threshold, and the π^0 may go on shell in the $D^0\bar{D}^{*0} - D^{*0}\bar{D}^0$ system. This calls for proper inclusion of the $D^0\bar{D}^0\pi^0$ three-body intermediate state [34–36]. Moreover, the inclusion of the $\bar{D}^{*0}$ and D^{*0} finite widths has a significant effect on the line shape of the $X(3872)$ [39–41]. In Refs. [42,43], a Galilean-invariant effective field theory for $X(3872)$ is developed to study the interplay between the $D^0\bar{D}^{*0} - D^{*0}\bar{D}^0$ and $D^0\bar{D}^0\pi^0$ components. A similar phenomenon happens in the case of newly observed double-charm $D^0D^{*+} - D^+D^{*0}$ molecule candidate T_{cc}^+ [44,45]. The effects of the three-body $DD\pi$ dynamics on the pole position of T_{cc}^+ and its line shape are first studied in Ref. [46], and then studied recently in Refs. [47,48]. In Refs. [49,50], the decay process $T_{cc}^+ \to D^0D^0\pi^+$ including the dynamical pion interaction is studied, the contributions from the triangle singularities generated from the π-exchange in this decay process are discussed in Ref. [49]. Thus, to understand the nature of the newly observed exotic states, such as $X(3872)$ and T_{cc}^+, it is necessary to study the analytic structure of the amplitude involving three-particle scattering.

The aim of this paper is to investigate the relativistic scattering involving three-particle interaction using the

*zhangxu@itp.ac.cn

isobar approximation [51–53] which respects constraints from two- and three-body unitarity. The specific system considered is the $D^0D^{*+} - D^+D^{*0}$, where the D^{*+} (D^{*0}) enters as a $D^+\pi^0$ or $D^0\pi^+$ ($D^0\pi^0$ or $D^+\pi^-$) resonance. We provide a detailed prescription for the analytic continuation of the amplitudes across the three-body and complex two-body unitarity cuts. Dynamical singularities emerged from π-exchange potential are stressed, and these singularities are inherent to three-body dynamics.

Much consideration has been given to the problem of calculating a relativistic three-body scattering within a unitary S-matrix theory in the past [51–59]. And some recent studies [60–64] extend these earlier works; new insights into covariant vs time-ordered formulations for the interaction kernel were obtained recently [65]; decay amplitudes with three particles in the final-state may be calculated using Khuri-Treiman equations [66–73], which contains particular realization of constrain from thee-body unitarity as shown in Refs. [67,68]. It turns out that the resulting equations are quite involved and demanding to solve.

Compared with the two-particle scattering, complications arise for the three-particle scattering not only because of the increase in the number of variables necessary to describe the processes, but also the possible appearance of the dynamic π-exchange, three-body, and complex two-body unitarity cuts as shown in analysis the cut structure of the amplitude within the S-matrix theory [74–76] and Faddeev equations [77,78]. Contour deformation of momentum has been employed as a solution tool necessary to analytically continue the amplitude into the unphysical region as shown in tracing the pole trajectory of three-neutron interaction [79] and describing the resonance pole generated from $\pi d - N\Delta$ interaction [80,81]. In Refs. [82–84], some aspects of this approach were discussed in detail in extracting the pole position of $a_1(1260)$ in a three-body unitary framework. We closely follow the approach in Refs. [79,80,83,84] and investigate the analytic continuation of the three-body $D^0D^{*+} - D^+D^{*0}$ scattering amplitude. In Refs. [85–87], similar three-body unitary formulations were developed to determine the pole positions of the resonances such as $\eta(1405/1475)$. Recently, in Ref. [88], a detailed and general prescription for analytic continuation of relativistic three-particle scattering amplitudes is studied, where the subsystem two-body interaction is described in the leading order effective range expansion.

The paper is organized as follows. In Sec. II, we present the integral equation for relativistic $D^0D^{*+} - D^+D^{*0}$ scattering which respects constraints from two- and three-body unitarity. The two-body subsystem $D^+\pi^0$ ($D^0\pi^+, D^0\pi^0, D^+\pi^-$) interacts via a separable interaction. In Sec. III, we construct the one-boson-exchange (OBE) potentials, which contain the σ, ρ, ω, and π-exchange. In Sec. IV, we present the prescription for the analytically continuation of the scattering amplitude into the unphysical region. In Sec. V, we present fitting results of the pole position generated from the integral equation and show its line shape in $D^0D^0\pi^+$ final state. In the last section, some conclusions are given.

II. THE BASIC FORMALISM

Since the D^{*0} and D^{*+} are unstable and have a width, they can never have an asymptotic state. In this work, we closely follow the isobar approach, the $D^0D^{*+} - D^+D^{*0}$ system is studied using a relativistic three-body equation, where the D^{*+} (D^{*0}) enters as a $D^+\pi^0$ or $D^0\pi^+$ ($D^0\pi^0$ or $D^+\pi^-$) resonance. Assuming only two- and three-body intermediate states, the form of the isobar propagator and the π-exchange potential are fixed by matching the effective Bethe-Salpeter (BS) equation with unitarity condition as derived in Refs. [51–53].

A. The coupled-channel $D^0D^{*+} - D^+D^{*0}$ scattering

We start by constructing the $D^0D^{*+} - D^+D^{*0}$ transition amplitude $T(s, p', p)$ in total angular momentum $J = 1$ nonperturbatively. Within the isobar approach, the $D^0D^{*+} - D^+D^{*0}$ interaction is constructed by an effective BS equation. The partial wave effective BS equation can be written as

$$T(s,p',p) = V(s,p',p) + \int_0^\Lambda \frac{k^2 dk}{(2\pi)^3 2\omega(k)} \times V(s,p',k)\tau(\sigma_k)T(s,k,p), \tag{1}$$

where

$$V(s,p',p) = \begin{pmatrix} V^{11}_{L'L}(s,p',p) & V^{12}_{L'L}(s,p',p) \\ V^{21}_{L'L}(s,p',p) & V^{22}_{L'L}(s,p',p) \end{pmatrix},$$
$$\tau(\sigma_k) = \begin{pmatrix} \tau^1(\sigma_k) & 0 \\ 0 & \tau^2(\sigma_k) \end{pmatrix}, \tag{2}$$

where, in each matrix element $V^{i'i}_{L'L}(s,p',p)$, the index $i(i') = 1,\ 2$ labels the particle channel ($D^0D^{*+} = 1$, $D^+D^{*0} = 2$) and $L(L')$ denotes the orbital angular momentum. The same structure holds for $T(s,p',p)$. The isobar propagator will be given in Sec. II B. The particles in channel 1 are

$$1 = D^{*+}, \qquad 2 = D^0, \tag{3}$$

and in channel 2 are

$$1 = D^{*0}, \qquad 2 = D^+. \tag{4}$$

The energy $\omega(k)$ is $\omega_{i,2}(k)$ in channel i, where $\omega_{i,j}(k) = \sqrt{m_{i,j}^2 + k^2}$ and j labels a particle. The incoming and outgoing momenta are denoted as p and p', s denotes the squared invariant mass of the three-body system, and σ_k

denotes the square of the four-momentum of the intermediate D^{*+} or D^{*0} subsystem,

$$\sigma_k = s - 2\sqrt{s}\omega_{i,2}(k) + m_{i,2}^2. \tag{5}$$

We take the masses of the mesons to be [31]

$$m_{D^0} = 1.86484\ \text{GeV}, \qquad m_{D^{*+}} = 2.01026\ \text{GeV},$$
$$m_{D^+} = 1.86966\ \text{GeV}, \qquad m_{D^{*0}} = 2.00685\ \text{GeV}. \tag{6}$$

The integrations in Eqs. (1) and (21) will be regularized by the same cutoff Λ in contrast to a form factor, since it simplifies the analytic continuation of the effective BS equation as discussed in Sec. IV.

As mentioned in the beginning of this section, in the present work only the part projected to total angular momentum $J = 1$, the quantum number of T_{cc}^+, is required. The term $V_{L'L}^{i'i}(s, p', p)$ in Eq. (2) represents the isobar-spectator potential with total angular momentum $J = 1$, and the index J has been suppressed. To obtain the partial wave interaction potentials in the JLS basis, we use the method given in Refs. [89,90]. First, in the helicity basis the relevant partial wave is extracted. We choose the incident $\vec{p}$ along the z-axis and outgoing $\vec{p}\,'$ to be in the x, z plane. The plane-wave isobar-spectator potential is related to the partial-wave potential as

$$V_{\lambda'\lambda}(s, \vec{p}\,', \vec{p}) = \frac{1}{4\pi}\sum_J (2J+1) d^J_{\lambda\lambda'}(\cos\theta) V^J_{\lambda'\lambda}(s, p', p), \tag{7}$$

where $\lambda(\lambda') = 0, \pm 1$ is the helicity eigenvalue of the spin-1 meson D^{*+} or D^{*0}, and θ is the angle between the outgoing momenta $\vec{p}\,'$ and incoming momenta $\vec{p}$.

Using the orthogonality relation for the Wigner $d^J_{\lambda\lambda'}(\cos\theta)$ functions,

$$\int_{-1}^{+1} d^J_{\lambda\lambda'}(\cos\theta) d^{J'}_{\lambda\lambda'}(\cos\theta) d\cos\theta = \frac{2}{2J+1}\delta_{JJ'}, \tag{8}$$

we can invert the above expression and obtain

$$V^J_{\lambda'\lambda}(s, p', p) = 2\pi \int_{-1}^{+1} d^J_{\lambda\lambda'}(\cos\theta) V_{\lambda'\lambda}(s, \vec{p}\,', \vec{p}) d\cos\theta. \tag{9}$$

Then, the transition from the helicity to the JLS representation is given by

$$V^J_{L'L}(s, p', p) = \sum_{\lambda'\lambda} \langle JL'S|J\lambda'\rangle V^J_{\lambda'\lambda}(s, p', p) \langle J\lambda|JLS\rangle, \tag{10}$$

where

$$U_{L\lambda} = \langle JLS|J\lambda\rangle = \sqrt{\frac{2L+1}{2J+1}} \langle L0S\lambda|J\lambda\rangle \langle S\lambda 00|S\lambda\rangle. \tag{11}$$

Here, J and S denote the total angular momentum and D^{*+} or D^{*0} spin, respectively. The symbols on the right-hand side are standard $SU(2)$ Clebsch-Gordan coefficients. In the present work, the $D^0D^{*+} - D^+D^{*0}$ system with quantum numbers $J^P = 1^+$, the spin and parity of T_{cc}^+, is considered. The allowed angular momentum is $L(L') =$ even number. We will only consider $L = L' = 0$. Then for $J = S = 1$, $L = 0$ and $\lambda = 0, \pm 1$, we get

$$\langle JLS|J\lambda\rangle = \frac{1}{\sqrt{3}}. \tag{12}$$

B. The isobar propagator

The isobar propagator for D^{*+} and D^{*0} is shown in Fig. 1. For the present work, we choose the renormalized isobar propagator

$$\tau^i(\sigma_k) = \frac{1}{\sigma_k - m_{i,1}^2 - \Sigma^R_{i,34}(\sigma_k) - \Sigma^R_{i,3'4'}(\sigma_k) + i m_{i,1}\Gamma_{i,\gamma} + i\epsilon}, \tag{13}$$

where

$$\Sigma^R_{i,jk}(\sigma_k) = \Sigma_{i,jk}(\sigma_k) - \text{Re}\Sigma^{\text{sub}}_{i,jk}(m_{i,1}^2), \tag{14}$$

and

$$\Sigma^{\text{sub}}_{i,jk}(m_{i,1}^2) = \Sigma_{i,jk}(m_{i,1}^2) + (\sigma_k - m_{i,1}^2) \times \left(\frac{d}{d\sigma_k}\Sigma_{i,jk}(\sigma_k)|_{\sigma_k = m_{i,1}^2}\right). \tag{15}$$

$\Gamma_{i,\gamma}$ is the radiative decay width of D^{*+} or D^{*0}. Since the radiative decay $D^{*0} \to D^0\gamma$ has a large branching ratio $\mathcal{B} \equiv \Gamma_{D^{*0},\gamma}/\Gamma_{D^{*0},\text{total}} = 35.3\%$ [31], we have included the radiative decay widths of D^{*+} and D^{*0}. To obtain the renormalized isobar propagator $\tau^i(\sigma_k)$ in Eq. (13), twice subtraction at the D^{*+} or D^{*0} physical mass has been used. The self-energy $\Sigma_{i,jk}(\sigma_k)$ is

$$\Sigma_{i,jk}(\sigma_k) = \int_0^\infty \frac{l^2 dl}{(2\pi)^3} \frac{\omega_{i,jk}(l)}{2\omega_{i,j}(l)\omega_{i,k}(l)} \frac{v_{ijk}(l)^2}{(\sigma_k - \omega_{i,jk}(l)^2 + i\epsilon)}, \tag{16}$$

where

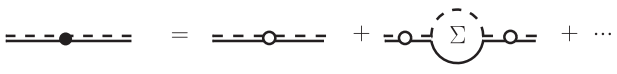

FIG. 1. A graphical representation of the isobar propagator of Eq. (13). The isobar propagator D^{*+} (D^{*0}) is dressed by an infinite number of $D^0\pi^+$ and $D^+\pi^0$ ($D^0\pi^0$ and $D^+\pi^-$) bubbles. The solid and dashed lines denote the $D^{0,+}$ and $\pi^{\pm,0}$, respectively.

$$\omega_{i,jk}(l) = \omega_{i,j}(l) + \omega_{i,k}(l), \tag{17}$$

where $j(k) = 3(4)$ or $3'(4')$ labels a particle, and the particles in channel 1 are

$$3 = D^0, \qquad 4 = \pi^+, \qquad 3' = D^+, \qquad 4' = \pi^0, \tag{18}$$

and in channel 2 are

$$3 = D^0, \qquad 4 = \pi^0, \qquad 3' = D^+, \qquad 4' = \pi^-. \tag{19}$$

The vertex $v_{ijk}(l)$ in the self-energy will be given in Eq. (26) in Sec. III A. The self-energy $\Sigma_{i,jk}(\sigma_k)$ contains the two-body intermediate state, and reflects the multi-Riemann sheet structure of the scattering amplitude. The prescription for the analytically continuation of the scattering amplitude into the unphysical region is presented in Sec. IV.

C. Three-body break-up production process in $D^0D^0\pi^+$ final state

Now, we calculate the three-body $D^0D^0\pi^+$ production rate using the constructed scattering amplitude $T(s, p', p)$. This quantity was measured by the LHCb Collaboration [44,45] and thus serves as an important link between theory and experiment. We consider a process in which T_{cc}^+ production at short ranges and subsequently decays to $D^0D^0\pi^+$. And as point out in Ref. [39], the short-range dynamics corresponding to T_{cc}^+ production can be absorbed into an overall coefficient $\mathcal{F}$.

In Fig. 2, we show a graphical representation for the T_{cc}^+ decay process. The production amplitude is separated into connected and disconnected parts using the LSZ reduction [91,92]. The decay amplitude $\mathcal{M}_{\Lambda\lambda}$ describes the T_{cc}^+ resonance at rest with helicity Λ measured along z axis into a D^0 and a $D^{*+} \to D^0\pi^+$ with helicity λ and can be written as [83,84,89,90]

$$\mathcal{M}_{\Lambda\lambda}(\vec{q}_1, \vec{q}_2, \vec{q}_3) = \frac{\mathcal{F}}{\sqrt{2}}\left[\sqrt{\frac{3}{4\pi}}\mathcal{D}^{1*}_{\Lambda\lambda}(\phi_1, \theta_1, 0)\mathcal{M}_L(q_1) \times U_{L\lambda}v_\lambda(\vec{q}_2, \vec{q}_3) + (\vec{q}_1 \leftrightarrow \vec{q}_2)\right], \tag{20}$$

and

$$\mathcal{M}_L(q_1) = \left(g_L^1 + \int_0^\Lambda \frac{p^2dp}{(2\pi)^3 2\omega_{D^0}(p)} g_{L'}^1 \tau^1(\sigma_p) T^{11}_{L'L}(p, q_1) + \int_0^\Lambda \frac{p^2dp}{(2\pi)^3 2\omega_{D^+}(p)} g_{L'}^2 \tau^2(\sigma_p) T^{21}_{L'L}(p, q_1)\right) \times \tau^1(\sigma_{q_1}), \tag{21}$$

this term is related to the decay amplitude in Eq. (20) by transforming back into plane waves and multiplying the final $D^{*+} \to D^0\pi^+$ vertex. Here, $\vec{q}_1$, and $\vec{q}_2$ are the outgoing D^0 momentum, and $\vec{q}_3$ is the outgoing π^+ momentum. $\mathcal{D}^{1*}_{\Lambda\lambda}(\phi_1, \theta_1, 0)$ denotes the capital Wigner-D function, with θ_1 and ϕ_1 giving the polar and azimuthal angles of $\vec{q}_1$, respectively. The vertex $v_\lambda(\vec{q}_2, \vec{q}_3) = -ig_{DD^*\pi}\epsilon^\mu_\lambda(\vec{q}_2 + \vec{q}_3)q_{3\mu}$ is given from the Lagrangian in Appendix A. The polarization vectors of the spin-1 particles are given in Appendix B. In addition, g_L^i is the effective coupling of T_{cc}^+ to channel i. In the exact isospin limit, one would have $g_L^1 = -g_L^2$ for an isoscalar state.

The production rate is given by a phase space integral over the decay amplitude, and can be written as

$$\frac{d\Gamma(\sqrt{s})}{d\sqrt{s}} = \int \frac{1}{(2\pi)^5}\frac{1}{16s}\left(\frac{1}{3}\sum_\Lambda |\sum_\lambda \mathcal{M}_{\Lambda\lambda}(\vec{q}_1, \vec{q}_2, \vec{q}_3)|^2\right) \times q_3^* q_1 dm_{23} d\Omega_3^* d\Omega_1, \tag{22}$$

where q_3^* and $\Omega_3^*(\theta_3^*, \phi_3^*)$ are the momentum and angle of particle 3 in the rest frame of particles 2 and 3, q_1 and $\Omega_1(\theta_1, \phi_1)$ are the momentum and angle of particle 1 in the rest frame of the decaying particle. The momentum q_3^* and q_1 are

$$q_3^* = \frac{\lambda^{1/2}(m_{23}^2, m_2^2, m_3^2)}{2m_{23}}, \qquad q_1 = \frac{\lambda^{1/2}(s, m_{23}^2, m_1^2)}{2\sqrt{s}}, \tag{23}$$

where

$$\lambda(x^2, y^2, z^2) = [x^2 - (y+z)^2][x^2 - (y-z)^2]. \tag{24}$$

When one exploits the azimuthal symmetry, the integral variable ϕ_1 is trivial. In our calculation, we integrate over four variables: m_{23}, θ_1, θ_3^* and ϕ_3^*.

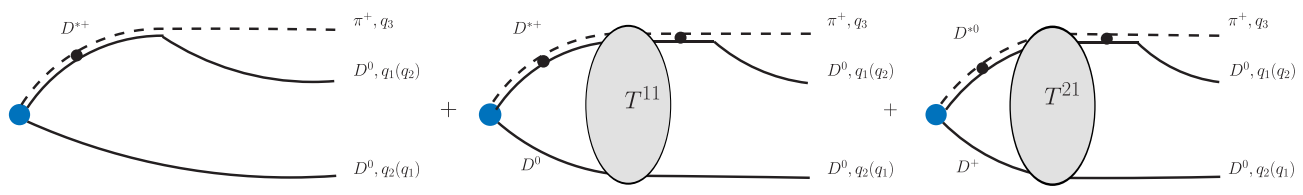

FIG. 2. Graphical representation for $D^0D^0\pi^+$ production. The short-range dynamics corresponding to T_{cc}^+ production can be absorbed to an overall coefficient $\mathcal{F}$.

III. THE INTERACTION POTENTIAL

In the present work, a crucial input is the interaction potentials between the charm mesons. The interaction potentials, which enter the effective BS equation, contain the σ, ρ and ω and π-exchange. The interaction potentials will be constructed with the help of effective Lagrangian given in Appendix A. For the σ, ρ, and ω-exchange, the interaction potentials will be constructed in a covariant form. For the π-exchange, the form of the interaction potential is derived from dispersive techniques as shown in Refs. [51–53]. Moreover, with the help of the effective Lagrangian, the two-body input $v_{ijk}(l)$ in the self-energy is given in Eq. (26).

A. Two-body subsystem interaction

The fundamental ingredient of the three-body theory developed in Sec. II is the assumption of an underlying separable two-body interaction. This implies that the two-body $D^+\pi^0$ or $D^0\pi^+$ ($D^0\pi^0$ or $D^+\pi^-$) scattering amplitude in total angular momentum $J_{\rm sub}=1$ channel is generated exclusively by a $D^{*+}(D^{*0})$ pole diagram. To obtain the partial wave projected vertex $v_{ijk}(p)$ in the self-energy in Eq. (16), we can consider the first-order Born series for the $j(p_j)k(p_k)\to j(p_j')k(p_k')$ scattering in two-body rest frame $p_j^{(\prime)}+p_k^{(\prime)}=(\sqrt{\sigma},0)$. This amplitude can be written as

$$\begin{aligned}\mathcal{A}(\sigma,z)&=I_f\cdot g^2_{\mathrm{DD}^*\pi}\frac{\sum_\lambda \epsilon_{\lambda,\mu}(p_j+p_k)p_k^\mu \epsilon^*_{\lambda,\nu}(p_j'+p_k')p_k^{\nu\prime}}{\sigma-m_{i,1}^2+i\epsilon}\\&=I_f\cdot g^2_{\mathrm{DD}^*\pi}\frac{pp'z}{\sigma-m_{i,1}^2+i\epsilon},\end{aligned}\tag{25}$$

where $z=\vec{p}\cdot\vec{p}\prime/pp'$, $p_j=(\omega_{i,j}(p),\vec{p})$, and analogous variables for p_k, p_j' and p_k'. I_f denotes the isospin factor. For $D^0\pi^+\to D^0\pi^+$ and $D^+\pi^0\to D^+\pi^0$ interactions, I_f are 1 and $\frac{1}{2}$, respectively. For $D^0\pi^0\to D^0\pi^0$ and $D^+\pi^-\to D^+\pi^-$ interactions, I_f are $\frac{1}{2}$ and 1, respectively. The second equal sign in Eq. (25) is due to the helicity sum. Projecting this amplitude to the P-wave amounts then to

$$\begin{aligned}\mathcal{A}^1(\sigma)&=2\pi\int_{-1}^{1}dzP_1(z)\mathcal{A}(\sigma,z)\\&=\frac{\left(g_{\mathrm{DD}^*\pi}\sqrt{\frac{4\pi}{3}I_f}\cdot p\right)\left(g_{\mathrm{DD}^*\pi}\sqrt{\frac{4\pi}{3}I_f}\cdot p'\right)}{\sigma-m_{i,1}^2+i\epsilon}\\&=\frac{v_{ijk}(p)v_{ijk}(p')}{\sigma-m_{i,1}^2+i\epsilon},\end{aligned}\tag{26}$$

and we obtain the projected vertex $v_{ijk}(p)$.

The two-body dynamics are encoded in $v_{ijk}(p)$, but also in the self-energy $\Sigma_{i,jk}(\sigma_k)$. The full two-body $j(p_j)k(p_k)\to j(p_j')k(p_k')$ scattering amplitude can be written as

$$\mathcal{A}(\sigma)=\frac{v_{ijk}(p)v_{ijk}(p')}{\sigma-m_{i,1}^2-\Sigma^R_{i,34}(\sigma)-\Sigma^R_{i,3'4'}(\sigma)+im_{i,1}\Gamma_{i,\gamma}+i\epsilon},\tag{27}$$

the renormalized self-energy is given in Eq. (14). It is obvious that in the three-body system, the two-body subsystem invariant mass is obtained by replacing $\sigma\to\sigma_k$, by the inclusion of the spectator D^0 or D^+.

B. The interaction potential

In this work, we consider two types of Feynman diagrams for meson exchange between the charm mesons as shown in Fig. 3. Then for coupled-channel $D^0D^{*+}-D^+D^{*0}$ interaction, with the Lagrangians given in Appendix A, the interaction potentials can be written as

$$\begin{aligned}\langle\vec{p}\prime\lambda'|V_{A-V}(E)|\vec{p}\lambda\rangle&=-g_{\mathrm{DDV}}\cdot g_{\mathrm{D}^*D^*V}\cdot IF\cdot(p_3+p_1)^\mu\frac{-g_{\mu\nu}+q_{1\mu}q_{1\nu}/m_V^2}{q_1^2-m_V^2+i\epsilon}(p_4+p_2)^\nu\epsilon^{*\alpha}_{\lambda'}(p_3)\epsilon_{\lambda\alpha}(p_1)+2g_{\mathrm{DDV}}\\&\cdot g'_{\mathrm{D}^*D^*V}\cdot IF\cdot[\epsilon^{*\mu}_{\lambda'}(p_3)\epsilon^\alpha_\lambda(p_1)q_{1\alpha}-\epsilon^{*\alpha}_{\lambda'}(p_3)\epsilon^\mu_\lambda(p_1)q_{1\alpha}]\frac{-g_{\mu\nu}}{q_1^2-m_V^2+i\epsilon}(p_4+p_2)^\nu,\end{aligned}\tag{28}$$

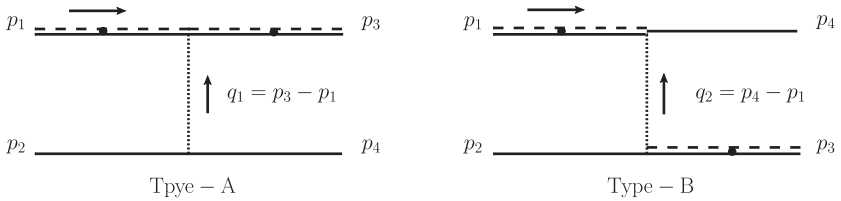

FIG. 3. Feynman diagrams for meson exchange between the charm mesons. The notations are the same as those in Fig. 1. The arrows denote the direction of momenta.

$$\langle \overrightarrow{p}\prime\lambda'|V_{B-V}(E)|\vec{p}\lambda\rangle = g^2_{\mathrm{DD}^*V}\cdot IF\cdot\varepsilon_{\alpha'\beta'\mu'\nu'}(p_3+p_2)^{\alpha'}q_2^{\beta'}\epsilon^{*\nu'}_{\lambda'}(p_3)\frac{-g_{\mu'\mu}}{q_2^2-m_V^2+i\epsilon}\varepsilon_{\alpha\beta\mu\nu}(p_4+p_1)^{\alpha}q_2^{\beta}\epsilon^{\nu}_{\lambda}(p_1), \tag{29}$$

$$\langle \overrightarrow{p}\prime\lambda'|V_{B-P}(E)|\vec{p}\lambda\rangle = g^2_{\mathrm{DD}^*\mathrm{P}}\cdot IF\cdot\epsilon^{*\nu}_{\lambda'}(p_3)q_{2\nu}\frac{\omega_{i,2}(p)+\omega_{i',2}(p')+\omega_P(q)}{\omega_P(q)[s-(\omega_{i,2}(p)+\omega_{i,2'}(p')+\omega_P(q))^2+i\epsilon]}\epsilon^{\mu}_{\lambda}(p_1)q_{2\mu}, \tag{30}$$

$$\langle \overrightarrow{p}\prime\lambda'|V_{A-S}(E)|\vec{p}\lambda\rangle = g_{\mathrm{D}^*D^*\sigma}g_{\mathrm{DD}\sigma}\epsilon^{*\mu}_{\lambda'}(p_3)\epsilon_{\lambda\mu}(p_1)\frac{1}{q_1^2-m_S^2+i\epsilon}, \tag{31}$$

with $\omega_P(q)=\sqrt{p^2+p'^2+m_P^2+2pp'\cos\theta}$, and V, P, and S denote the exchanged vector $\rho^{0,\pm}$, pseudoscalar $\pi^{0,\pm}$, and scalar σ mesons, respectively. The four-momentum of the incoming and outgoing particles are $p_1=(\sqrt{s}-\omega_{i,2}(p),\vec{p})$, $p_2=(\omega_{i,2}(p),-\vec{p})$, $p_3=(\sqrt{s}-\omega_{i',2}(p'),\overrightarrow{p}\prime)$, and $p_4=(\omega_{i',2}(p'),-\overrightarrow{p}\prime)$. The four-momentum of the exchanged mesons are $q_1=p_3-p_1$ for type-A diagram, and $q_2=p_4-p_1$ for type-B diagram. The isospin factors IF for type-A and type-B diagrams are given in Table I. We can see a cancellation between the neutral ρ^0 and ω exchange potentials in both type-A and type-B diagrams. And only the charged $\rho^{\pm}$ and $\pi^{0,\pm}$-exchange potentials contribute. Then we build DD^* isoscalar $I=0$ and isovector $I=1$ combinations as

$$|DD^*,I=0\rangle = -\frac{1}{\sqrt{2}}(D^{*+}D^0-D^{*0}D^+),$$
$$|DD^*,I=1\rangle = -\frac{1}{\sqrt{2}}(D^{*+}D^0+D^{*0}D^+). \tag{32}$$

IV. ANALYTIC PROPERTIES OF THE INTEGRAL EQUATION

Contour deformation of momentum has been employed as a solution tool necessary to analytically continue the amplitude into the unphysical region as shown in tracing the pole trajectory of three-neutron interaction [79] and describing the resonance pole generated from πd-$N\Delta$ interaction [80,81]. Via complex momentum contour deformation, the π-exchange cut can be avoided and the analytic domain of the effective BS equation kernel is extended. The method of constructing suitable contours to access the Riemann sheet(s) of interest, was detailed discussed in extracting the pole position of $a_1(1260)$ within a three-body unitary framework in Refs. [83,84]. We closely follow the approach in Refs. [79,80,83,84] and investigate the analytic continuation of the three-body $D^0D^{*+}-D^+D^{*0}$ scattering amplitude.

TABLE I. The isospin factors IF for type-A and type-B diagrams and different exchange mesons.

	Type-A			Type-B				
	ρ^0	$\rho^{\pm}$	ω	ρ^0	$\rho^{\pm}$	ω	π^0	$\pi^{\pm}$
$1\to1$	$\frac{1}{2}$	$\cdots$	$-\frac{1}{2}$	$\cdots$	1	$\cdots$	$\cdots$	1
$2\to2$	$\frac{1}{2}$	$\cdots$	$-\frac{1}{2}$	$\cdots$	1	$\cdots$	$\cdots$	1
$1\to2$	$\cdots$	-1	$\cdots$	$-\frac{1}{2}$	$\cdots$	$\frac{1}{2}$	$-\frac{1}{2}$	$\cdots$

Two types of integrations occur: (i) in $k:=|\vec{k}|$ within the effective BS equation in Eq. (1) and (ii) in $l:=|\vec{l}|$ within the self-energy term of the two-body subsystem in Eq. (13). The corresponding integral contours can be chosen individually and are refereed to in the following as as "spectator momentum contour" (denoted by Γ_{spe}) and "self-energy contour" (denoted by Γ_{sef}), respectively. Both contours start at the respective origins, $k=l=0$, and end at $k=\Lambda$ and $l=\infty$, respectively. In between these limits, different choices of the contours define different Riemann sheets in $\sqrt{s}$ as talked in the following.

A. Analytical continuation of the self-energy

As a function of energy $\sqrt{\sigma}$, the self-energy $\Sigma_{i,jk}(\sigma)$ in Eq. (16) is no longer single valued. We must therefore place the complex $\sqrt{\sigma}$ plane by a Riemann surface of multisheet, the different Riemann sheets are connected by a branch cut. A branch point defines the thresholds, and at which a cut begins is fixed. This is illustrated in Fig. 4 above threshold at $\sqrt{\sigma}=m_{i,3}+m_{i,4}$. The placement of contour Γ_{sef} producing physical amplitude is constrained by the $+i\epsilon$ in Eq. (16). In the figure, choosing the integral contour passing the singularity at $l_{cm}+i\epsilon$ on the right (Γ_R),

$$l_{cm}=\frac{\lambda^{1/2}(\sigma,m_{i,3}^2,m_{i,4}^2)}{2\sqrt{\sigma}}, \tag{33}$$

yields a self-energy on the physical Riemann sheet. In contrast, choosing the integral contour passing the singularity at $l_{cm}+i\epsilon$ on the left (Γ_L) leads to a sign change in $\mathrm{Im}\Sigma_{i,jk}(\sigma)$ and a self-energy on the unphysical Riemann sheet. The self-energy on physical Riemann sheet in the upper half-plane of $\sqrt{\sigma}$ is connected along the real axis, $\sqrt{\sigma}\in[m_{i,3}+m_{i,4},\infty)$, to the unphysical Riemann sheet in the lower half-plane. For the energy $\mathrm{Im}\sqrt{\sigma}<0$ (lower right in Fig. 4), the self-energy on unphysical Riemann sheet can be obtained by deforming the contour Γ_{sef} as shown to the

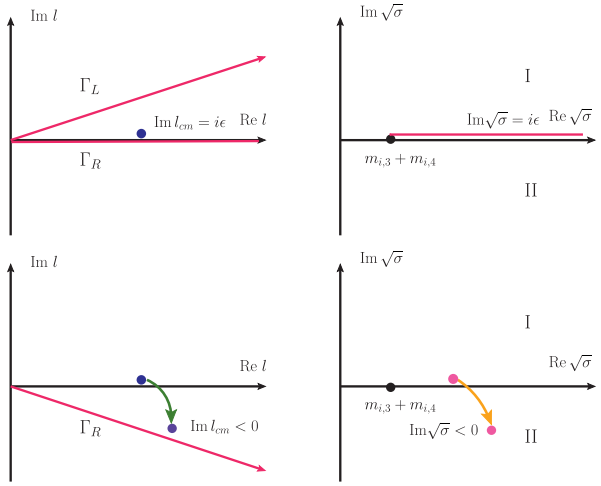

FIG. 4. Integration contours for the self-energy in Eq. (16). Upper row: momentum integral contour (left panel) and the physical Riemann sheet of the self-energy at $\sqrt{\sigma} + i\epsilon$ (right panel). Lower row: integral contour along the red line (left panel) and the unphysical Riemann sheet of the self-energy at $\mathrm{Im}\sqrt{\sigma} < 0$ (right panel).

lower left in Fig. 4. In particular, the singularity at l_{cm} also acquires a negative imaginary part, but a smooth deformation of Γ_R ensures that the contour Γ_{sef} still passes the singularity to the right. This guarantees that the self-energy has been analytically continued from physical Riemann sheet to the unphysical Riemann sheet in the lower half-plane, where the resonance resides.

To display the contour Γ_{sef} and the pole position of D^{*+} (D^{*0}) resonance evaluated from Eq. (27) in the same plot, the contour Γ_{sef} is mapped to the $\sqrt{\sigma}$ plane according to $\sqrt{\sigma} = [\omega_{i,j}(l) + \omega_{i,k}(l)]^{1/2}$. In Fig. 5, the pink and green lines in lower left panel (lower right panel) correspond to the integral contours for $D^0\pi^+$ and $D^+\pi^0$ ($D^0\pi^0$ and $D^+\pi^-$) self-energies, respectively. The pole position of D^{*+} (D^{*0}) at $\sqrt{\sigma}$ plane is shown in the upper left panel (upper right panel) of Fig. 5. One can see as the $D^0\pi^+$ and $D^+\pi^0$ channels are on their unphysical Riemann sheets, the pole position of D^{*+} evaluated from Eq. (27) is at

$$\mathrm{Re}m^p_{D^{*+}} = m_{D^{*+}}, \qquad \mathrm{Im}m^p_{D^{*+}} = -43.5\ \mathrm{keV}. \tag{34}$$

As the $D^0\pi^0$ and $D^+\pi^-$ channels are on their unphysical Riemann sheets, the pole position of D^{*0} evaluated from Eq. (27) is at

$$\mathrm{Re}m^p_{D^{*0}} = m_{D^{*0}}, \qquad \mathrm{Im}m^p_{D^{*0}} = -32.5\ \mathrm{keV}. \tag{35}$$

B. Singularities in the π-exchange potential

Apart from singularities in two-body subsystem amplitude, there are singularities in the π-exchange potential. The singularity occurs when the denominator of Eq. (30) vanishes for any $x \equiv \cos\theta \in [-1, 1]$ according to the partial wave decomposition of Eq. (9). For a fixed three-body energy $\sqrt{s}$ and outgoing spectator momentum p', the singularities are given by

$$k_\pm = \frac{2\alpha p' x \pm \sqrt{4\alpha^2 p'^2 x^2 + (\beta^2 - 4p'^2x^2)(\alpha^2 - \beta^2 m^2_{i,2})}}{(\beta^2 - 4p'^2x^2)}, \tag{36}$$

where

$$\begin{aligned} \alpha &= m_\pi^2 - s - m^2_{i,2} - m^2_{i',2} + 2\sqrt{s}\omega_{i',2}(p'), \\ \beta &= 2\omega_{i',2}(p') - 2\sqrt{s}, \end{aligned} \tag{37}$$

and m_π is the exchanged π^0 or $\pi^\pm$ mass. In Fig. 6, as an example we show the positions of the singularities of k for a fixed p', $\sqrt{s}$ and $x \equiv \cos\theta \in [-1, 1]$ for solution of $k_\pm$ in Eq. (36). In the complex k plane, as $0 < p' < p'_1$ (left panel in Fig. 6), the singularities are located in the first and third quadrants. Increasing the value of p', as $p'_1 < p' < p'_2$ (medium panel in Fig. 6), a circular cut arises from the π-exchange potential. The circular cut grows with the increase of the value of p'. Still increasing the value of p', as $p'_2 < p'$ (right panel in Fig. 6), the circular cut opens. Here p'_1 and p'_2 are

$$\begin{aligned} p'_1 &= \frac{\lambda^{1/2}((\sqrt{s} - m_{i,2})^2, m^2_{i',2}, m^2_\pi)}{2(\sqrt{s} - m_{i,2})}, \\ p'_2 &= \frac{\lambda^{1/2}(s, (m_\pi + m_{i,2})^2, m^2_{i',2})}{2\sqrt{s}}. \end{aligned} \tag{38}$$

C. Continuation across the three-body and complex two-body cuts

To explore the region of the complex $\sqrt{s}$ plane where the T^+_{cc} is located, the amplitude $T(s, p', p)$ can be analytically continued into the unphysical Riemann sheets via the deformation of the integration contour. We make the transformation [79–81]

$$p' \to p' e^{-i\theta}, \qquad k \to k e^{-i\theta}, \tag{39}$$

with $0 < \theta < \frac{\pi}{2}$. As shown in the left panel in Fig. 6, the integration contour can be chosen along the orange line. Since both p' and k in Eq. (1) are rotated by a same angle θ, the potential $V(s, p', k)$ does not create any problem in rotating the contour of integration. And we only need to examine how the singularities from $\tau^i(\sigma_k)$ effect the contour rotation.

For two-body scattering, with a choice of the l contour along the real axis, the self-energy appearing in Eq. (27) has a well-known right-hand cut along the real $\sqrt{\sigma}$ axis starting at $\sqrt{\sigma} = m_{i,3} + m_{i,4}$. In the three-body case, the effective

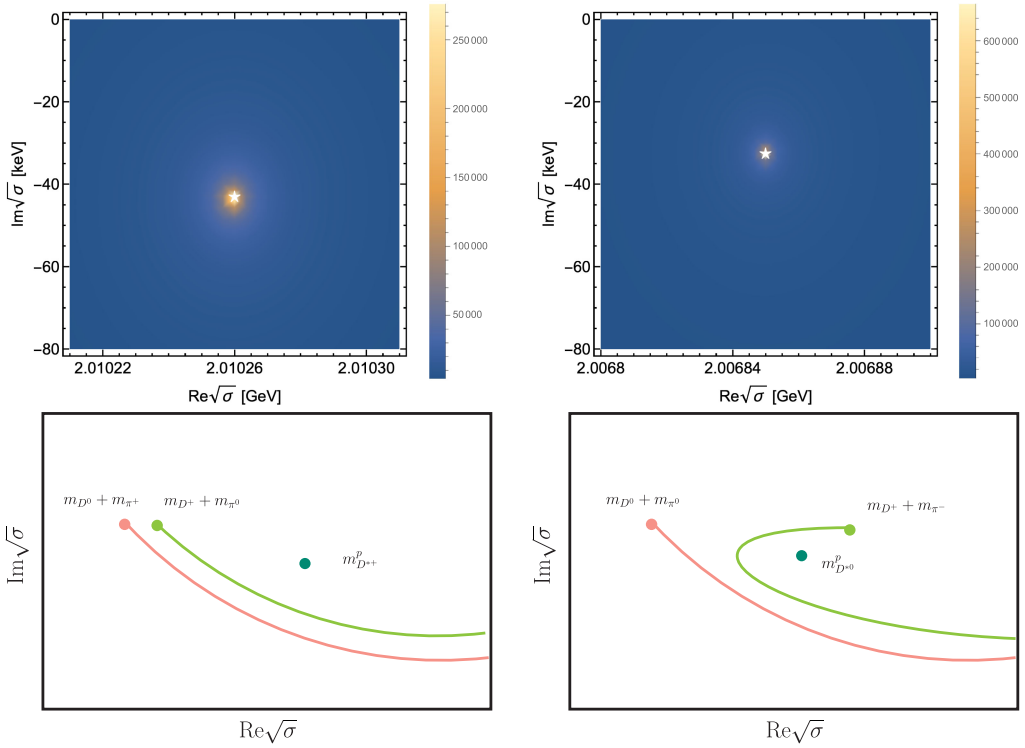

FIG. 5. Upper row: the pole position of D^{*+} (D^{*0}) at the $\sqrt{\sigma}$ plane. The D^{*+} (D^{*0}) pole at $\sqrt{\sigma}$ plane is highlighted with the white star in the left (right) panel. Lower row: example for the contours $\Gamma_{\rm sef}$ in the complex $\sqrt{\sigma}$ plane. The pink and green lines in left (right) panel correspond to the integral contours for $D^0\pi^+$ and $D^+\pi^0$ ($D^0\pi^0$ and $D^+\pi^-$) self-energies, respectively.

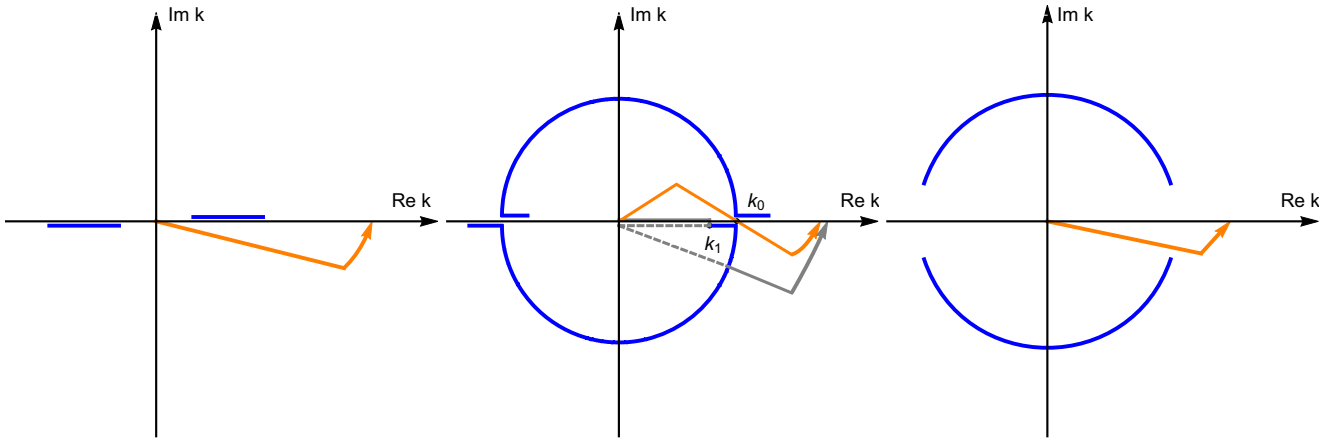

FIG. 6. The blue lines are positions of the singularities of k for a fixed p', $\sqrt{s}$ and $x \equiv \cos\theta \in [-1, 1]$ for the solution of $k_\pm$ in Eq. (36). In the medium panel, the momentum k_0 is the position where the contour is squeezed between the logarithmic cuts. The k_1 is the endpoint of the circular cut k_- in Eq. (36) by setting $x = +1$.

BS equation has a three-body cut generated by the self-energy appearing in the denominator of $\tau^i(\sigma_k)$ in Eq. (13). And this cut is given by

$$\sigma_k - \omega_{i,jk}(l)^2 = 0, \tag{40}$$

where σ_k and $\omega_{i,jk}(l)$ are given in Eqs. (5) and (17), respectively. For real k and a l contour following the real axis this equation defines a cut along the real $\sqrt{s}$ axis starting at $2m_{D^0} + m_{\pi^+}$ ($m_{D^0} + m_{D^+} + m_{\pi^0}$ and $2m_{D^+} + m_{\pi^-}$). These three-body cuts are indicated in Fig. 7 with the orange dashed lines along the real $\sqrt{s}$ axis.

We take the analytic continuation of the amplitude $T(s, p', p)$ across the three-body $D^0D^0\pi^+$ cut as an example. By deforming the integration contour, the amplitude $T(s, p', p)$ can be analytically continued across the

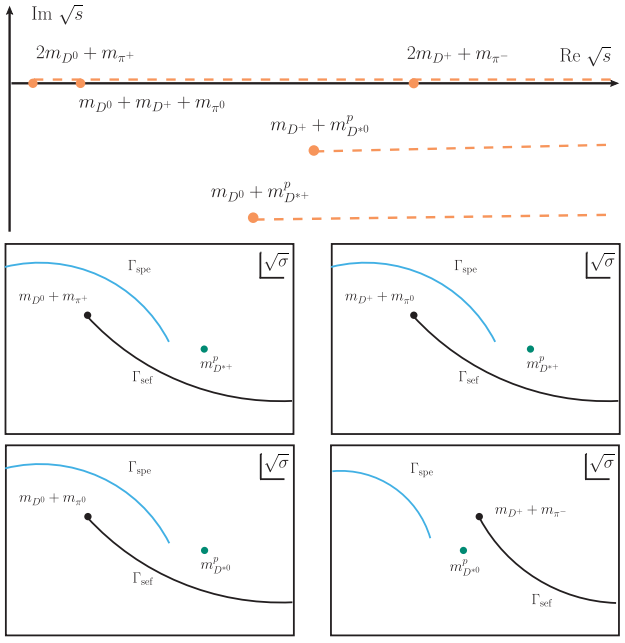

FIG. 7. Analytic structure of the three-body amplitude in the $\sqrt{s}$ plane. The real and complex branch points (orange dots) are shown together with their respective cuts (orange dashed lines). The inserts show the contours $\Gamma_{\rm spe}$ mapped to the $\sqrt{\sigma}$ plane (blue lines), in a qualitative way. In the $\sqrt{\sigma}$ plane, the contours $\Gamma_{\rm sef}$ (black lines) starting at the two-body thresholds (black dots) do not change if $\sqrt{s}$ changes, but the contours $\Gamma_{\rm spe}$ do.

$D^0D^0\pi^+$ cut, for $\mathrm{Im}\sqrt{s}<0$ and $\mathrm{Re}\sqrt{s}>2m_{D^0}+m_{\pi^+}$. The inserts in Fig. 7 show the $\sqrt{\sigma}$ plane with the contours $\Gamma_{\rm spe}$ and $\Gamma_{\rm sef}$. The position of the inserts in the $\sqrt{s}$ plane qualitatively corresponds to $\sqrt{s}$ used to map the contour $\Gamma_{\rm spe}$ to the $\sqrt{\sigma}$ plane, via Eq. (5). Note the position of the contour $\Gamma_{\rm spe}$ relative to the $D^0\pi^+$ branch point at $m_{D^0}+m_{\pi^+}$ and D^{*+} pole at $m^p_{D^{*+}}$ (upper left insert in Fig. 7). Moreover, there is no across between the contours $\Gamma_{\rm spe}$ and $\Gamma_{\rm sef}$ in $\sqrt{\sigma}$ plane. This ensures that the integrand is always analytic. With the similar method, the amplitude $T(s,p',p)$ can be analytically continued across the three-body $D^0D^+\pi^0$ or $D^+D^+\pi^-$ cut.

Other singularities appear at the zero of the denominator of Eq. (13),

$$\sigma_k - m^2_{i,1} - \Sigma^{R,\mathrm{II}}_{i,34}(\sigma_k) - \Sigma^{R,\mathrm{II}}_{i,3'4'}(\sigma_k) + i m_{i,1}\Gamma_{i,\gamma} = 0. \tag{41}$$

Note that the self-energies are evaluated on their unphysical Riemann sheets. The pole positions of the resonances D^{*+} and D^{*0} are given by Eqs. (34) and (35), respectively. Using $\sqrt{\sigma_k}=\sqrt{s}-m_{i,2}$ at $k=0$, we obtain the positions of the complex branch points at complex $\sqrt{s}$ plane,

$$\sqrt{s} = m^p_{i,1} + m_{i,2}, \tag{42}$$

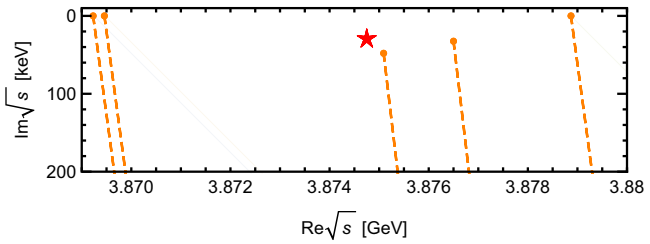

FIG. 8. The cut structure of the effective BS equation in complex $\sqrt{s}$ plane for the momentum contour rotated by an angle of $\theta=\pi/8$ in Eq. (39). The real and complex branch points (orange dots) are shown together with their respective cuts (orange dashed lines). The T^+_{cc} pole observed by the LHCb Collaboration at $\sqrt{s}$ plane is highlighted with the red star.

where $m^p_{i,1}$ is the pole position of D^{*+} or D^{*0}. Thus, the complex branch points in $\sqrt{s}$ plane are directly related to the poles of the unstable particles.

Translated into complex k plane, the singularities corresponding to the vanishing of denominator of Eq. (13) are at

$$k_b = \frac{\lambda^{1/2}(s,(m^p_{i,1})^2,m^2_{i,2})}{2\sqrt{s}}. \tag{43}$$

For $\mathrm{Re}\sqrt{s}>m_{i,1}+m_{i,2}$, and $\mathrm{Im}\sqrt{s}<\mathrm{Im}m^p_{i,1}$, those branch points are in the fourth quadrant of the k plane and at an angle of ϕ_b, where

$$\tan\phi_b = \frac{\mathrm{Im}k_b}{\mathrm{Re}k_b}. \tag{44}$$

Thus, as far as the complex branch point is concerned, we can take $\theta>|\phi_b|$ in Eq. (39) to analytically continue the amplitude $T(s,p',p)$ into another unphysical Riemann sheet. See Refs. [80,81] for a more detailed discussion.

In Fig. 8, we show the cut structure of the effective BS equation in complex $\sqrt{s}$ plane for the momentum contour rotated by an angle of $\theta=\pi/8$ in Eq. (39). From Fig. 8, it is clear we have extended the energy domain over which $T(s,p',p)$ is defined to that part of the unphysical Riemann sheet where resonances are normally located. As shown in the complex $\sqrt{s}$ plane, the T^+_{cc} pole is always to the left of the complex branch points at $m^p_{D^{*+}}+m_{D^0}$ and $m^p_{D^{*0}}+m_{D^+}$, to the right of the branch points at $2m_{D^0}+m_{\pi^+}$ and $m_{D^0}+m_{D^+}+m_{\pi^0}$, and to the left of the branch point at $2m_{D^+}+m_{\pi^-}$. Therefore, the qualitative positions of $\Gamma_{\rm spe}$ and contours $\Gamma_{\rm sef}$ in the $\sqrt{\sigma}$ plane, corresponding to $\sqrt{s}$ taking the value of T^+_{cc} pole, are given by the inserts in Fig. 7. The contours $\Gamma_{\rm spe}$ pass both the D^{*+} and D^{*0} poles to the left. Both the $D^0\pi^+$ and $D^+\pi^0$ self-energy contours $\Gamma_{\rm sef}$ pass the D^{*+} pole on the right. The $D^0\pi^0$ and $D^+\pi^-$ self-energy contours $\Gamma_{\rm sef}$ pass the D^{*0} pole on the right and left, respectively.

D. The $T(s,p',p)$ for real momentum p and p'

The effective BS equation is solved numerically by replacing the integrals by sums using Gaussian quadratures and inverting the resulting matrix equation [93]. The number of Gauss points determines the numerical precision of this method. We have checked, a 140-point Gaussian quadrature yields accurate results in this work.

To obtain $T(s,p',p)$ for real momentum p and p', a major difficulty in doing this is the treatment of the singularities of the kernel. These arise both from the isobar propagator and the π-exchange potential. In the present work, we use the contour deformation method developed in Refs. [94–97]. Some formal aspects of this method were also described in detail in Appendix B in Ref. [98]. The method consists of two steps. First, the analytically continuation of the effective BS equation for complex momentum is made. The effective BS equation is solved for complex momenta which is free from singularities. Then the solution for real momenta is obtained using Cauchy's theorem, starting with the solution for complex momenta. For example, as in the Appendix B in Ref. [98], taking the initial and final momenta p and k' to be real, the Eq. (B1) can be used for a second time to get the solution for real momenta. The integration path C is along the chosen contour as before for accessing the solution for complex momenta.

Here, we would like to describe the detailed treatment of the singularities of the potential $V^{i'i}_{L'L}(s,p',p)$ having the configuration shown in Fig. 6. For $0 < p' < p'_1$ (left panel in Fig. 6), and for $p'_2 < p'$ (right panel in Fig. 6), the integration contours can be chosen along the orange lines in the fourth quadrant of the complex k plane. For $p'_1 < p' < p'_2$ (medium panel in Fig. 6), integration contour may be chosen along the gray line. It is important that when integrating along this contour, one has to go onto the second sheet of $V^{i'i}_{L'L}(s,p',p)$ (dashed line part in the medium panel in Fig. 6). And the knowledge of the amplitude $T(s,p',p)$ in the interval $[0,k_1]$ is needed, where $k_1 = k_-(x=+1)$ in Eq. (36). However, one can find that the inequality $p'_1 > k_1$ does not always hold in this work. In the present work, for $p'_1 < p' < p'_2$, we use another integration contour (the orange line in the medium panel in Fig. 6). This contour has been employed in Refs. [96,99]. The potentials $V^{i'i}_{L'L}(s,p',p)$ are always calculated on the physical Riemann sheet. A certain disadvantage of this method lies in the fact that the position of the momentum k_0, where the contour is squeezed between the logarithmic cuts, depends on the value of the momentum p'. For this reason one has to solve the set of equation separately for each value of p' of the chosen mesh.

V. NUMERICAL RESULTS AND DISCUSSION

In the following we present the results of the approach in terms of the line shape $\frac{d\Gamma(\sqrt{s})}{d\sqrt{s}}$ calculated from Eq. (22). The free parameters of the model are the cutoff Λ and the overall normalization factor $\mathcal{F}$. The two parameters are fixed by a fitting to the $D^0D^0\pi^+$ line shape obtained by the LHCb Collaboration [44,45]. When fitting the LHCb data, the coupling constants g^i_L can be absorbed into the overall factor $\mathcal{F}$. To take into account the experimental resolution, the line shape $\frac{d\Gamma(\sqrt{s})}{d\sqrt{s}}$ in Eq. (22) is convolved with an energy resolution function,

$$\frac{d\tilde{\Gamma}(\sqrt{s})}{d\sqrt{s}} = \int d\sqrt{s'} R_{\rm LHCb}(\sqrt{s},\sqrt{s'}) \frac{d\Gamma(\sqrt{s'})}{d\sqrt{s'}}. \tag{45}$$

The resolution function $R_{\rm LHCb}(\sqrt{s},\sqrt{s'})$ is parametrized by a sum of two Gaussian functions,

$$R_{\rm LHCb}(\sqrt{s},\sqrt{s'}) = \sum_{i=1,2} \alpha_i \frac{1}{\sqrt{2\pi}\sigma_i} \exp\left(-\frac{(\sqrt{s'}-\sqrt{s})^2}{2\sigma_i^2}\right), \tag{46}$$

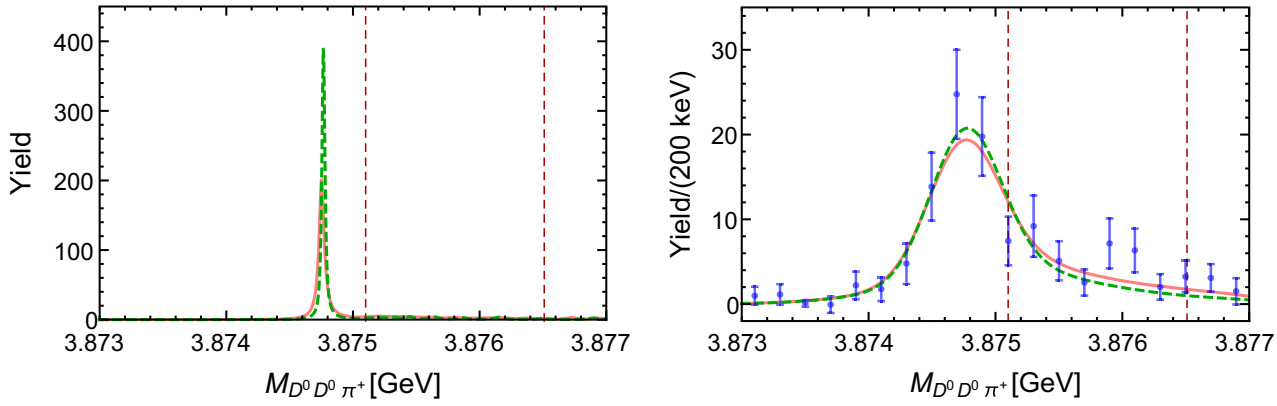

FIG. 9. Fitting results of the $D^0D^0\pi^+$ line shapes before (left panel) and after (right panel) convolution with the energy resolution function. The green dashed and pink lines correspond to schemes I and II, respectively. The vertical dashed lines represent the D^0D^{*+} and D^+D^{*0} thresholds. The experimental binning with the bin size of 200 keV is included in the fits.

TABLE II. The values of the parameters Λ and the pole positions from fitting of the $D^0D^0\pi^+$ line shape obtained by the LHCb Collaboration. The pole positions are given relative to the D^0D^{*+} threshold. The uncertainties of the cutoff Λ are obtained by χ^2 fitting to the LHCb data and propagate to the pole position.

Scheme	χ^2/d.o.f.	Λ GeV	$\sqrt{s_{\rm pole}^{\rm thr}}$ keV
I	$18.11/(20-1)=0.95$	0.4551 ± 0.0018	$-332^{+37}_{-36}-i(18\pm1)$
II	$14.47/(20-1)=0.76$	0.3701 ± 0.0017	$-351^{+37}_{-35}-i(28\pm1)$

TABLE III. The effective coupling constants extracted as defined in Eq. (47).

Scheme	g^1	g^2	$g^{I=0}$	$g^{I=1}$
I	$3.90^{+0.09}_{-0.09}-i0.04^{+0.00}_{-0.00}$	$-4.11^{+0.09}_{-0.09}+i0.04^{+0.00}_{-0.00}$	$-5.66^{+0.13}_{-0.13}+i0.06^{+0.00}_{-0.00}$	$0.15^{+0.00}_{-0.00}+i0.00^{+0.00}_{-0.00}$
II	$4.00^{+0.09}_{-0.09}+i0.04^{+0.00}_{-0.00}$	$-4.13^{+0.09}_{-0.09}+i0.05^{+0.00}_{-0.00}$	$-5.75^{+0.13}_{-0.13}+i0.01^{+0.00}_{-0.00}$	$0.09^{+0.00}_{-0.00}-i0.07^{+0.00}_{-0.00}$

where $\alpha_1=0.778$, $\alpha_2=0.222$, $\sigma_1=1.05\times263$ keV, $\sigma_2=2.413\sigma_1$ [45].

In order to investigate the role played by the π-exchange potential, we consider the following two different fit schemes:

(i) Scheme I: The OBE potentials excluding π-exchange potential.
(ii) Scheme II: The full dynamical calculation, the π-exchange potential is included.

Once the cutoff Λ is fixed through the fit to the experimental data, the position of the pole of the amplitude can be searched in the complex energy $\sqrt{s}$ plane. The physical T_{cc}^+ signal is associated with the corresponding pole in the $D^0D^{*+}-D^+D^{*0}$ scattering amplitude $T(s,p',p)$. The effective coupling g^i to channel i can be obtained from the residue of the amplitude $T(s,p',p)$ at the pole position,

$$g^{i'}g^i=\lim_{s\to s_{\rm pole}}\frac{1}{4\pi}(s-s_{\rm pole})T^{i'i}(s,k_b,k_b), \quad (47)$$

and the on shell momentum k_b is given in Eq. (43).

The fitted line shapes for the two schemes are shown in Fig. 9. The parameters of the fits and extracted pole positions are given in Table II. These fitting quantities can be assessed through the corresponding values of χ^2/d.o.f. given in Table II. The fitting results of the two schemes are comparable.

The three-body and complex two-body cuts imply the multi-Riemann sheets of the amplitude $T(s,p',p)$. As shown in Fig. 8, in the energy near the T_{cc}^+ pole, the $D^0D^0\pi^+$ and $D^+D^0\pi^0$ channels are on their unphysical Riemann sheets, while the $D^+D^+\pi^-$ is on its physical Riemann sheet. In scheme I, where OBE potentials excluding π-exchange potential, the position of the pole is at $\sqrt{s_{\rm pole}^{\rm thr}}=-332^{+37}_{-36}-i(18\pm1)$ keV. In scheme II, where the π-exchange potential is included, the position of the pole is at $\sqrt{s_{\rm pole}^{\rm thr}}=-351^{+37}_{-35}-i(28\pm1)$ keV. The width of T_{cc}^+ in scheme II is larger than in scheme I by a factor of 1.5. Our results indicate that the inclusion of π-exchange mainly influences the width of T_{cc}^+. For a bound state with a small binding energy, the π-exchange can be dealt with using perturbation theory. This is agreement with the findings in Refs. [32,35,36,42].

In Table III, we show the values of the effective coupling constants to different channels obtained from Eq. (47). In the exact isospin limit, one would have $g_L^1=-g_L^2$ ($g_L^1=g_L^2$) for an isoscalar (isovector) state. We find that the coupling constants g_L^1 and g_L^2 are very close to each other with an opposite sign. This indicates that we have basically a state with an isospin $I=0$. The values of the coupling constants obtained here are similar to those obtained in Refs. [46,100,101].

VI. SUMMARY

In this work, we discussed the analytic continuation of the three-body $D^0D^{*+}-D^+D^{*0}$ scattering amplitude $T(s,p',p)$. Compared with the two-particle scattering, complications arise for the three-particle scattering not only because of the increase in the number of variables necessary to describe the processes, but also the possible appearance of the dynamic π-exchange, three-body and complex two-body unitarity cuts. In particular, we find that the logarithmic singularities of the π-exchange potential can form into a circular cut. Via the contour deformation, this cut can be circumvented, and the integration of the effective BS equation does not pose any numerical problem.

Employing the contour deformation, the effective BS equation can be analytically continued to the unphysical region. As we have shown, one can choose a self-consistent integration contour, which defines a smooth continuation of

the amplitude to the domain of analyticity. As an implementation, we find the π-exchange term has a significant effect on the pole position of the T_{cc}^{+}. Including the π-exchange term, the width of T_{cc}^{+} will be increased by a factor of 1.5.

Systematic analysis the newly observed hadronic states requires building the amplitude that satisfies the constrains such as unitarity and analyticity. The present work discussed the prescription for solving and analytically continuing the effective BS equation describing the three-body reactions. Such an analysis is expected to provide an important theoretical background for determining the parameters of the newly exotic candidates. In the near future, we will extend our framework to calculate the $3\pi - K\overline{K}\pi$ coupled system suggested to be responsible for the exotic candidate $a_1(1420)$ [102–105].

ACKNOWLEDGMENTS

I would like to thank Feng-Kun Guo for fruitful and enlightening discussions and comments. Also I would like to thank Jia-Jun Wu for useful discussions regarding the circular cut. The results described in this paper are supported by HPC Cluster of ITP-CAS. This work is supported in part by the National Natural Science Foundation of China (NSFC) under Grants No. 12247139, by the Chinese Academy of Sciences under Grants No. XDB34030000 and No. YSBR-101; by the National Key R&D Program of China under Grant No. 2023YFA1606703.

APPENDIX A: THE INTERACTION LAGRANGIAN

The interaction Lagrangian between pseudo-Goldstone bosons and the mesons containing a heavy quark can be constructed by imposing invariance under both heavy quark spin-flavor transformation and chiral transformation [106–110]. The light vector mesons nonet can be introduced by using the hidden gauge symmetry approach [110–112]. The Lagrangian containing these particles can be written as

$$\begin{aligned}
\mathcal{L}_{DD^*P} &= g_{DD^*P}(D_b D_a^{*\mu\dagger} + D_b^{*\mu} D_a^{\dagger})(\partial_\mu \mathcal{M})_{ba} + g_{\bar{D}\bar{D}^*P}(\bar{D}_a^{*\mu\dagger}\bar{D}_b + \bar{D}_a^{\dagger}\bar{D}_b^{*\mu})(\partial_\mu \mathcal{M})_{ab},\\
\mathcal{L}_{\mathrm{DDV}} &= ig_{DDV}(D_b \overleftrightarrow{\partial_\mu} D_a^{\dagger})V_{ba}^{\mu} + ig_{\bar{D}\,\bar{D}\,V}(\bar{D}_b \overleftrightarrow{\partial_\mu} \bar{D}_a^{\dagger})V_{ab}^{\mu},\\
\mathcal{L}_{D^*D^*V} &= ig_{D^*D^*V}(D_{b\nu}^{*} \overleftrightarrow{\partial_\mu} D_a^{*\nu\dagger})V_{ba}^{\mu} + ig'_{D^*D^*V}(D_b^{*\mu} D_a^{*\nu\dagger} - D_a^{*\mu\dagger} D_b^{*\nu})(\partial_\mu V_\nu - \partial_\nu V_\mu)_{ba}\\
&\quad + ig_{\bar{D}^*\bar{D}^*V}(\bar{D}_{b\nu}^{*} \overleftrightarrow{\partial_\mu} \bar{D}_a^{*\nu\dagger})V_{ab}^{\mu} + ig'_{\bar{D}^*\bar{D}^*V}(\bar{D}_b^{*\mu}\bar{D}_a^{*\nu\dagger} - \bar{D}_a^{*\mu\dagger}\bar{D}_b^{*\nu})(\partial_\mu V_\nu - \partial_\nu V_\mu)_{ab},\\
\mathcal{L}_{D^*DV} &= ig_{D^*DV}\varepsilon_{\lambda\alpha\beta\mu}(D_b \overleftrightarrow{\partial}^{\lambda} D_a^{*\mu\dagger} + D_b^{*\mu} \overleftrightarrow{\partial}^{\lambda} D_a^{\dagger})(\partial^\alpha V^\beta)_{ba} + ig_{\bar{D}^*\bar{D}V}\varepsilon_{\lambda\alpha\beta\mu}(\bar{D}_b \overleftrightarrow{\partial}^{\lambda} \bar{D}_a^{*\mu\dagger} + \bar{D}_b^{*\mu} \overleftrightarrow{\partial}^{\lambda} \bar{D}_a^{\dagger})(\partial^\alpha V^\beta)_{ba}.
\end{aligned} \tag{A1}$$

The matrix $\mathcal{M}$ contains π, K, η fields, which is a 3×3 Hermitian and traceless matrix. V_μ is analogous to $\mathcal{M}$ containing ρ, K^*, ω and ϕ. The matrix $\mathcal{M}$ and V_μ are expressed as

$$\mathcal{M} = \begin{pmatrix} \frac{\pi^0}{\sqrt{2}} + \frac{\eta}{\sqrt{6}} & \pi^+ & K^+ \\ \pi^- & -\frac{\pi^0}{\sqrt{2}} + \frac{\eta}{\sqrt{6}} & K^0 \\ K^- & \bar{K}^0 & -\sqrt{\frac{2}{3}}\eta \end{pmatrix},$$

$$V = \begin{pmatrix} \frac{\rho^0}{\sqrt{2}} + \frac{\omega}{\sqrt{2}} & \rho^+ & K^{*+} \\ \rho^- & -\frac{\rho^0}{\sqrt{2}} + \frac{\omega}{\sqrt{2}} & K^{*0} \\ K^{*-} & \bar{K}^{*0} & \phi \end{pmatrix}. \tag{A2}$$

The isospin doublets are $D = (D^+, -D^0)$ and $D^* = (D^{*+}, -D^{*0})$. The coupling constants are as follows,

$$\begin{aligned}
g_{DD^*P} &= -g_{\bar{D}\bar{D}^*P} = -\frac{2g}{f_\pi}\sqrt{M_D M_{D^*}},\\
g_{DDV} &= -g_{\bar{D}\,\bar{D}\,V} = \frac{1}{\sqrt{2}}\beta g_V,\\
g_{D^*D^*V} &= -g_{\bar{D}^*\bar{D}^*V} = -\frac{1}{\sqrt{2}}\beta g_V,\\
g'_{D^*D^*V} &= -g'_{\bar{D}^*\bar{D}^*V} = -\sqrt{2}\lambda g_V M_{D^*},\\
g_{DD^*V} &= g_{\bar{D}\bar{D}^*V} = \sqrt{2}\lambda g_V.
\end{aligned} \tag{A3}$$

The effective Lagrangian between σ and heavy mesons are

$$\begin{aligned}
\mathcal{L}_{DD\sigma} &= g_{DD\sigma} D_a D_a^{\dagger}\sigma + g_{\bar{D}\,\bar{D}\,\sigma}\bar{D}_a\bar{D}_a^{\dagger}\sigma,\\
\mathcal{L}_{D^*D^*\sigma} &= g_{D^*D^*\sigma} D_a^{*\mu} D_{a\mu}^{*\dagger}\sigma + g_{\bar{D}^*\bar{D}^*\sigma}\bar{D}_a^{*\mu}\bar{D}_{a\mu}^{*\dagger}\sigma,
\end{aligned} \tag{A4}$$

and the relevant coupling constants are

$$\begin{aligned}
g_{DD\sigma} &= g_{\bar{D}\,\bar{D}\,\sigma} = -2g_\sigma M_D,\\
g_{D^*D^*\sigma} &= g_{\bar{D}^*\bar{D}^*\sigma} = 2g_\sigma M_{D^*}.
\end{aligned}$$

In this work, we choose the coupling constants $g = 0.59$, $g_V = 5.8$, $\beta = 0.9$, $\lambda = 0.56\ \mathrm{GeV}^{-1}$, $f_\pi = 0.132$ GeV, and $g_\sigma = 0.76$ as in Refs. [109,113].

APPENDIX B: THE POLARIZATION VECTORS AND KINEMATICS

Spin-1 helicity polarization vectors are given by

$$\epsilon_0^\mu(p) = \frac{1}{m}\begin{pmatrix} |\vec{p}| \\ E\sin\theta\cos\phi \\ E\sin\theta\sin\phi \\ E\cos\theta \end{pmatrix}, \qquad \epsilon_{\pm1}^\mu(p) = \frac{1}{\sqrt{2}}\begin{pmatrix} 0 \\ \mp\cos\theta\cos\phi + i\sin\phi \\ \mp\cos\theta\sin\phi - i\cos\phi \\ \pm\sin\theta \end{pmatrix}, \tag{B1}$$

where $p^\mu = (E, \vec{p})$ is the particle four-momentum, m is the particle mass and

$$\vec{p} = (|\vec{p}|\sin\theta\cos\phi, |\vec{p}|\sin\theta\sin\phi, |\vec{p}|\cos\theta). \tag{B2}$$

The helicity sum gives

$$\sum_\lambda \epsilon_{\lambda,\mu}(p)\epsilon^*_{\lambda,\nu}(p) = -g_{\mu\nu} + \frac{p_\mu p_\nu}{m^2}. \tag{B3}$$

[1] A. Hosaka, T. Iijima, K. Miyabayashi, Y. Sakai, and S. Yasui, Prog. Theor. Exp. Phys. **2016**, 062C01 (2016).
[2] R. F. Lebed, R. E. Mitchell, and E. S. Swanson, Prog. Part. Nucl. Phys. **93**, 143 (2017).
[3] A. Esposito, A. Pilloni, and A. D. Polosa, Phys. Rep. **668**, 1 (2017).
[4] F.-K. Guo, C. Hanhart, U.-G. Meißner, Q. Wang, Q. Zhao, and B.-S. Zou, Rev. Mod. Phys. **90**, 015004 (2018); **94**, 029901(E) (2022).
[5] S. L. Olsen, T. Skwarnicki, and D. Zieminska, Rev. Mod. Phys. **90**, 015003 (2018).
[6] Y.-R. Liu, H.-X. Chen, W. Chen, X. Liu, and S.-L. Zhu, Prog. Part. Nucl. Phys. **107**, 237 (2019).
[7] N. Brambilla, S. Eidelman, C. Hanhart, A. Nefediev, C.-P. Shen, C. E. Thomas, A. Vairo, and C.-Z. Yuan, Phys. Rep. **873**, 1 (2020).
[8] F.-K. Guo, X.-H. Liu, and S. Sakai, Prog. Part. Nucl. Phys. **112**, 103757 (2020).
[9] G. Yang, J. Ping, and J. Segovia, Symmetry **12**, 1869 (2020).
[10] M. Y. Barabanov *et al.*, Prog. Part. Nucl. Phys. **116**, 103835 (2021).
[11] X.-K. Dong, F.-K. Guo, and B.-S. Zou, Commun. Theor. Phys. **73**, 125201 (2021).
[12] H.-X. Chen, W. Chen, X. Liu, Y.-R. Liu, and S.-L. Zhu, Rep. Prog. Phys. **86**, 026201 (2023).
[13] M. Mai, U.-G. Meißner, and C. Urbach, Phys. Rep. **1001**, 1 (2023).
[14] S. Durr *et al.* (BMW Collaboration), Science **322**, 1224 (2008).
[15] J. J. Dudek, R. G. Edwards, C. E. Thomas, and D. J. Wilson (Hadron Spectrum Collaboration), Phys. Rev. Lett. **113**, 182001 (2014).
[16] R. Williams, C. S. Fischer, and W. Heupel, Phys. Rev. D **93**, 034026 (2016).
[17] M. E. Carrillo-Serrano, W. Bentz, I. C. Cloët, and A. W. Thomas, Phys. Rev. C **92**, 015212 (2015).
[18] G. Eichmann, H. Sanchis-Alepuz, R. Williams, R. Alkofer, and C. S. Fischer, Prog. Part. Nucl. Phys. **91**, 1 (2016).
[19] C. T. Johnson and J. J. Dudek (Hadron Spectrum Collaboration), Phys. Rev. D **103**, 074502 (2021).
[20] L. Gayer, N. Lang, S. M. Ryan, D. Tims, C. E. Thomas, and D. J. Wilson (Hadron Spectrum Collaboration), J. High Energy Phys. 07 (2021) 123.
[21] N. Lang and D. J. Wilson (Hadron Spectrum Collaboration), Phys. Rev. Lett. **129**, 252001 (2022).
[22] R. E. Peierls, Proc. R. Soc. A **253**, 16 (1959).
[23] R. G. Newton, J. Math. Phys. (N.Y.) **1**, 319 (1960).
[24] J. Gunson and J. G. Taylor, Phys. Rev. **119**, 1121 (1960).
[25] R. Oehme, Phys. Rev. **121**, 1840 (1961).
[26] R. Blankenbecler, M. L. Goldberger, S. W. MacDowell, and S. B. Treiman, Phys. Rev. **123**, 692 (1961).
[27] W. R. Frazer and A. W. Hendry, Phys. Rev. **134**, B1307 (1964).
[28] R. J. Eden and J. R. Taylor, Phys. Rev. **133**, B1575 (1964).
[29] M. Kato, Ann. Phys. (N.Y.) **31**, 130 (1965).

[30] J. R. Taylor, *Scattering Theory: The Quantum Theory of Nonrelativistic Collisions* (John Wiley & Sons, Inc., New York, 1972).
[31] R. L. Workman *et al.* (Particle Data Group), Prog. Theor. Exp. Phys. **2022**, 083C01 (2022).
[32] S. Fleming, M. Kusunoki, T. Mehen, and U. van Kolck, Phys. Rev. D **76**, 034006 (2007).
[33] L. Dai, F.-K. Guo, and T. Mehen, Phys. Rev. D **101**, 054024 (2020).
[34] M. Suzuki, Phys. Rev. D **72**, 114013 (2005).
[35] V. Baru, A. A. Filin, C. Hanhart, Y. S. Kalashnikova, A. E. Kudryavtsev, and A. V. Nefediev, Phys. Rev. D **84**, 074029 (2011).
[36] M. Schmidt, M. Jansen, and H. W. Hammer, Phys. Rev. D **98**, 014032 (2018).
[37] D. B. Kaplan, M. J. Savage, and M. B. Wise, Phys. Lett. B **424**, 390 (1998).
[38] D. B. Kaplan, M. J. Savage, and M. B. Wise, Nucl. Phys. **B34**, 329 (1998).
[39] E. Braaten and M. Lu, Phys. Rev. D **76**, 094028 (2007).
[40] E. Braaten and J. Stapleton, Phys. Rev. D **81**, 014019 (2010).
[41] C. Hanhart, Y. S. Kalashnikova, and A. V. Nefediev, Phys. Rev. D **81**, 094028 (2010).
[42] E. Braaten, Phys. Rev. D **91**, 114007 (2015).
[43] E. Braaten, L.-P. He, and J. Jiang, Phys. Rev. D **103**, 036014 (2021).
[44] R. Aaij *et al.* (LHCb Collaboration), Nat. Phys. **18**, 751 (2022).
[45] R. Aaij *et al.* (LHCb Collaboration), Nat. Commun. **13**, 3351 (2022).
[46] M.-L. Du, V. Baru, X.-K. Dong, A. Filin, F.-K. Guo, C. Hanhart, A. Nefediev, J. Nieves, and Q. Wang, Phys. Rev. D **105**, 014024 (2022).
[47] L. Qiu, C. Gong, and Q. Zhao, arXiv:2311.10067.
[48] J.-Z. Wang, Z.-Y. Lin, and S.-L. Zhu, arXiv:2309.09861.
[49] N. N. Achasov and G. N. Shestakov, Phys. Rev. D **105**, 096038 (2022).
[50] L. Dai, S. Fleming, R. Hodges, and T. Mehen, Phys. Rev. D **107**, 076001 (2023).
[51] R. Blankenbecler and R. Sugar, Phys. Rev. **142**, 1051 (1966).
[52] R. Aaron, R. D. Amado, and J. E. Young, Phys. Rev. **174**, 2022 (1968).
[53] R. Aaron *et al.*, *Modern Three-Hadron Physics* (Springer-Verlag, Berlin, Heidelberg and New York, 1977).
[54] R. Blankenbecler, Phys. Rev. **122**, 983 (1961).
[55] L. F. Cook and B. W. Lee, Phys. Rev. **127**, 283 (1962).
[56] G. N. Fleming, Phys. Rev. **135**, B551 (1964).
[57] M. T. Grisaru, Phys. Rev. **146**, 1098 (1966).
[58] R. Aaron and R. D. Amado, Phys. Rev. Lett. **31**, 1157 (1973).
[59] R. D. Amado, Phys. Rev. Lett. **33**, 333 (1974).
[60] M. Mai, B. Hu, M. Doring, A. Pilloni, and A. Szczepaniak, Eur. Phys. J. A **53**, 177 (2017).
[61] A. Jackura, C. Fernández-Ramírez, V. Mathieu, M. Mikhasenko, J. Nys, A. Pilloni, K. Saldaña, N. Sherrill, and A. P. Szczepaniak (JPAC Collaboration), Eur. Phys. J. C **79**, 56 (2019).
[62] M. Mikhasenko, Y. Wunderlich, A. Jackura, V. Mathieu, A. Pilloni, B. Ketzer, and A. P. Szczepaniak, J. High Energy Phys. 08 (2019) 080.
[63] A. W. Jackura, S. M. Dawid, C. Fernández-Ramírez, V. Mathieu, M. Mikhasenko, A. Pilloni, S. R. Sharpe, and A. P. Szczepaniak, Phys. Rev. D **100**, 034508 (2019).
[64] S. M. Dawid and A. P. Szczepaniak, Phys. Rev. D **103**, 014009 (2021).
[65] X. Zhang, C. Hanhart, U.-G. Meißner, and J.-J. Xie, Eur. Phys. J. A **58**, 20 (2022).
[66] N. N. Khuri and S. B. Treiman, Phys. Rev. **119**, 1115 (1960).
[67] I. J. R. Aitchison and R. Pasquier, Phys. Rev. **152**, 1274 (1966).
[68] R. Pasquier and J. Y. Pasquier, Phys. Rev. **170**, 1294 (1968).
[69] F. Niecknig and B. Kubis, J. High Energy Phys. 10 (2015) 142.
[70] F. Niecknig and B. Kubis, Phys. Lett. B **780**, 471 (2018).
[71] T. Isken, B. Kubis, S. P. Schneider, and P. Stoffer, Eur. Phys. J. C **77**, 489 (2017).
[72] J. Gasser and A. Rusetsky, Eur. Phys. J. C **78**, 906 (2018).
[73] M. Albaladejo, D. Winney, I. V. Danilkin, C. Fernández-Ramírez, V. Mathieu, M. Mikhasenko, A. Pilloni, J. A. Silva-Castro, and A. P. Szczepaniak (JPAC Collaboration), Phys. Rev. D **101**, 054018 (2020).
[74] R. C. Hwa, Phys. Rev. **130**, 2580 (1963).
[75] R. C. Hwa, Phys. Rev. **134**, B1086 (1964).
[76] M. Rubin, R. Sugar, and G. Tiktopoulos, Phys. Rev. **146**, 1130 (1966).
[77] D. D. Brayshaw, Phys. Rev. **176**, 1855 (1968).
[78] D. D. Brayshaw and R. F. Peierls, Phys. Rev. **177**, 2539 (1969).
[79] W. Glockle, Phys. Rev. C **18**, 564 (1978).
[80] B. C. Pearce and I. R. Afnan, Phys. Rev. C **30**, 2022 (1984).
[81] I. R. Afnan, Aust. J. Phys. **44**, 201 (1991).
[82] G. Janssen, K. Holinde, and J. Speth, Phys. Rev. C **49**, 2763 (1994).
[83] D. Sadasivan, M. Mai, H. Akdag, and M. Döring, Phys. Rev. D **101**, 094018 (2020); **103**, 019901(E) (2021).
[84] D. Sadasivan, A. Alexandru, H. Akdag, F. Amorim, R. Brett, C. Culver, M. Döring, F. X. Lee, and M. Mai, Phys. Rev. D **105**, 054020 (2022).
[85] S. X. Nakamura, Q. Huang, J. J. Wu, H. P. Peng, Y. Zhang, and Y. C. Zhu, Phys. Rev. D **109**, 014021 (2024).
[86] S. X. Nakamura, Q. Huang, J. J. Wu, H. P. Peng, Y. Zhang, and Y. C. Zhu, Phys. Rev. D **107**, L091505 (2023).
[87] S. X. Nakamura, X. H. Li, H. P. Peng, Z. T. Sun, and X. R. Zhou, arXiv:2312.17658.
[88] S. M. Dawid, M. H. E. Islam, and R. A. Briceño, Phys. Rev. D **108**, 034016 (2023).
[89] M. Jacob and G. C. Wick, Ann. Phys. (N.Y.) **7**, 404 (1959).
[90] S. U. Chung, 10.5170/CERN-1971-008 (1971).
[91] C. Itzykson and J. B. Zuber, *Quantum Field Theory*, International Series in Pure and Applied Physics (McGraw-Hill, New York, 1980).
[92] H. Lehmann, K. Symanzik, and W. Zimmermann, Nuovo Cimento **1**, 205 (1955).

[93] M. I. Haftel and F. Tabakin, Nucl. Phys. **A58**, 1 (1970).
[94] J. H. Hetherington and L. H. Schick, Phys. Rev. **137**, B935 (1965).
[95] R. Aaron and R. D. Amado, Phys. Rev. **150**, 857 (1966).
[96] R. T. Cahill and I. H. Sloan, Nucl. Phys. **A65**, 161 (1971); **A96**, 632(E) (1972).
[97] E. Schmid and H. Ziegelmann, *The Quantum Mechanical Three-Body Problem* (Pergamon Press, Oxford, 1974).
[98] X. Zhang, H.-L. Fu, F.-K. Guo, and H.-W. Hammer, Phys. Rev. C **108**, 044304 (2023).
[99] A. Fix and H. Arenhövel, Phys. Rev. C **100**, 034003 (2019).
[100] A. Feijoo, W. H. Liang, and E. Oset, Phys. Rev. D **104**, 114015 (2021).
[101] M. Albaladejo, Phys. Lett. B **829**, 137052 (2022).
[102] C. Adolph *et al.* (COMPASS Collaboration), Phys. Rev. Lett. **115**, 082001 (2015).
[103] M. Mikhasenko, B. Ketzer, and A. Sarantsev, Phys. Rev. D **91**, 094015 (2015).
[104] F. Aceti, L. R. Dai, and E. Oset, Phys. Rev. D **94**, 096015 (2016).
[105] G. D. Alexeev *et al.* (COMPASS Collaboration), Phys. Rev. Lett. **127**, 082501 (2021).
[106] G. Burdman and J. F. Donoghue, Phys. Lett. B **280**, 287 (1992).
[107] M. B. Wise, Phys. Rev. D **45**, R2188 (1992).
[108] T.-M. Yan, H.-Y. Cheng, C.-Y. Cheung, G.-L. Lin, Y. C. Lin, and H.-L. Yu, Phys. Rev. D **46**, 1148 (1992); **55**, 5851 (E) (1997).
[109] A. F. Falk and M. E. Luke, Phys. Lett. B **292**, 119 (1992).
[110] R. Casalbuoni, A. Deandrea, N. Di Bartolomeo, R. Gatto, F. Feruglio, and G. Nardulli, Phys. Rep. **281**, 145 (1997).
[111] R. Casalbuoni, A. Deandrea, N. Di Bartolomeo, R. Gatto, F. Feruglio, and G. Nardulli, Phys. Lett. B **299**, 139 (1993).
[112] R. Casalbuoni, A. Deandrea, N. Di Bartolomeo, R. Gatto, F. Feruglio, and G. Nardulli, Phys. Lett. B **292**, 371 (1992).
[113] C. Isola, M. Ladisa, G. Nardulli, and P. Santorelli, Phys. Rev. D **68**, 114001 (2003).